A&A manuscript no.
(will be inserted by hand later)

Your thesaurus codes are:
04(04.19.1; 03.20.1; 08.16.4; 13.19.5; 10.19.2)

ASTRONOMY AND ASTROPHYSICS

February 1, 2008

The ATCA/VLA OH 1612 MHz survey. III. Observations of the Northern Galactic Plane.

M.N. Sevenster[1], H.J. van Langevelde[2], R.A. Moody[1], J.M. Chapman[3], H.J. Habing[4] and N.E.B. Killeen[3]

[1] MSSSO/RSAA, Cotter Road, Weston ACT 2611, Australia (msevenst@mso.anu.edu.au)
[2] Joint Institute for VLBI in Europe, Postbus 2, 7990 AA Dwingeloo, The Netherlands
[3] Australia Telescope National Facility, P.O.Box 76, Epping NSW 1710, Australia
[4] Sterrewacht Leiden, P.O. Box 9513, 2300 RA Leiden, The Netherlands

Received ; accepted

arXiv:astro-ph/0011259v1 14 Nov 2000

Abstract. We present observations of the region between $5° \leq \ell \leq 45°$ and $|b| \leq 3°$, in the OH 1612.231 MHz line, taken from 1993 to 1995 with NRAO's Very Large Array [1] (VLA). These observations are the last part of a larger survey, covering $|\ell| \leq 45°$ and $|b| \leq 3°$, with the Australia Telescope Compact Array (ATCA) and the VLA. The region was systematically observed on a $30'\times30'$ grid in (ℓ, b) and the resulting coverage was 92% , with 965 pointings. We found 286 OH–masing objects, 161 of which are new detections and 207 have reliable IRAS point–source identifications. The outflow velocity was determined for 276 sources. A total of 766 sources were detected in the combined ATCA/VLA survey, of which 29 were detected in two regions of the survey.

The source tables and spectra (Table 2 and Fig. 10 can be downloaded from http://msowww.anu.edu.au∼msevenst/pubs.html

In this article we analyse the data statistically and give identifications with known sources where possible. The "efficiency" of this VLA survey is 75% of that of the ATCA Bulge survey. This efficiency was determined by comparing the detections in the region where the two surveys overlap. The completeness– and error characteristics are similar, though less homogeneous, except for the much larger errors in the flux densities. The relatively large surface number density found in the northern disk, suggests that we can see the Bar extending to higher longitudes on this side of the galactic Centre.

1. Introduction

We have surveyed a large section of the galactic plane in the OH 1612–MHz satellite line. The aim of the survey was to sample the stellar dynamics in the plane, cutting through the major components of the Galaxy. Very strong radiation is emitted in the observed OH line by, amongst others, OH/IR stars (for a review see Habing 1996). These are particularly suitable tracers of the stellar dynamics for a variety of reasons. Most important is that they are easily observable in any region of the Galaxy, their line–of–sight velocity can be determined very accurately and they represent a large fraction of the stellar population. This article is the sequel to previous articles discussing the Australia Telescope Compact Array (ATCA) "Bulge" ($|\ell|<10°$, Sevenster et al. 1997a, Paper I) and "Disk" ($\ell<-10°$, Sevenster et al. 1997b, Paper II) parts of the survey. Here we discuss the results of the northern plane region, between $5° \leq \ell \leq 45°$ and $|b| \leq 3°$. This region was observed with the VLA in New Mexico.

We discuss the observations in Sect. 2 and the data reduction in Sect. 3. In Sect. 4 we give the results of this survey and in Sect. 5 a statistical analysis of the data, that, like Paper II, follows closely the analysis in Paper I. We summarize in Sect. 6.

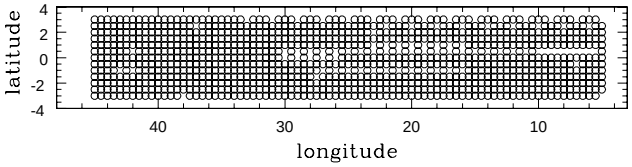

Fig. 1. The 965 pointings of the VLA survey that were used in the data reduction; no data were obtained for 88 pointings out of 1053. In reality the maps were square ($41'\times41'$ in α, δ) and overlapping. A single missing pointing (of which there are 50, cf. around ℓ=42°) leaves a hole of $\sim10'\times10'$ in the coverage, but influences the sensitivity in a larger area.

Send offprint requests to: M. Sevenster

[1] The National Radio Astronomy Observatory is a facility of the National Science Foundation operated under cooperative agreement by Associated Universities, Inc.

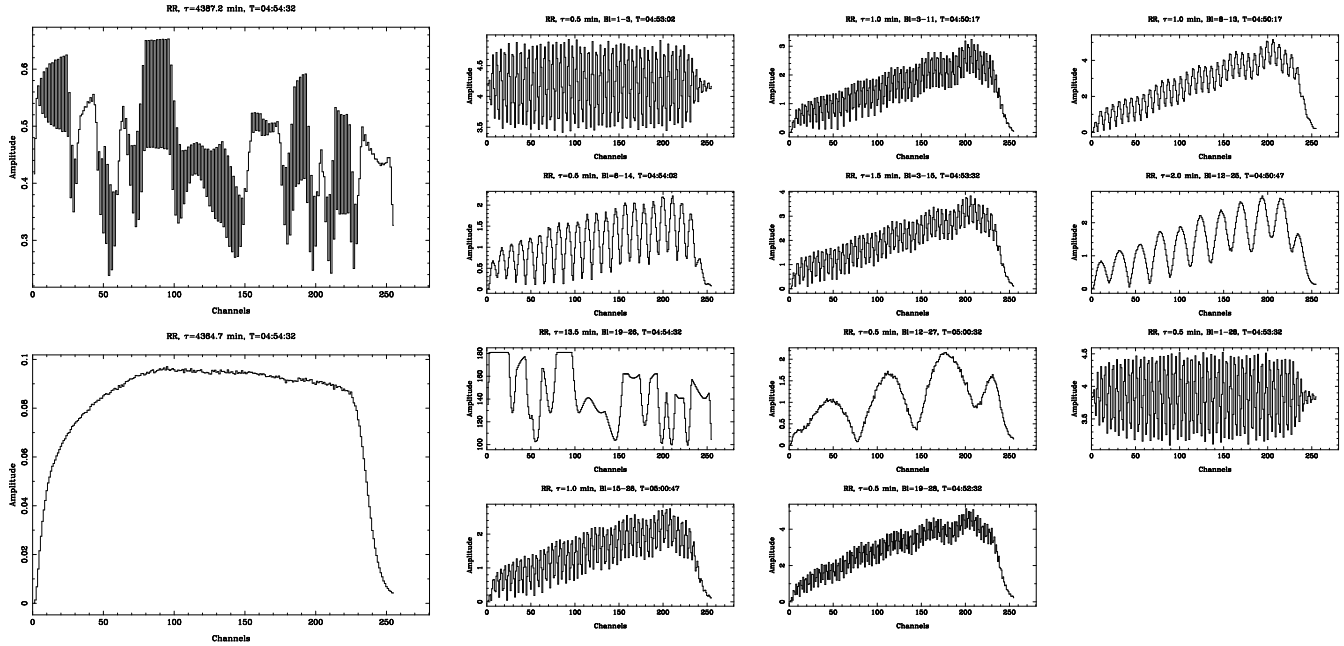

Fig. 2. a–c. The two larger panels on the left show the raw spectrum of a primary calibrator (1331+305), taken on 210594, averaged over all baselines (top) and after flagging with WSRFI (bottom). The smaller panels on the right show the single–integration, single–baseline spectra (ie. visibilities) that were actually flagged by WSRFI. Most of these visibilities were flagged as 'G' (Sect. 3.1), except for the 7th plot, which was a 'W'.

Table 1. All observing runs, with array configuration, RFI type (Sect. 3.1), maximum baseline length (ranging with observing direction and time of day) and number of useful fields in the run.

Date	Array	RFI TYPES	UVMAX	N
200293	AB	G	75-110	73
080693	BC	W,G,S^{206}	30-37	71
090693	C	W,G,S^{206}	16-18	70
100693	C	G	17-18	70
310893	C	G,S^{226}	7-12	73
020993	CD	W,G	7-12	46
090993	CD	W,G,S^{226}	7-12	72
210594	AB	W,G,S^{210}	100-120	38
260594	AB	W,G	70-120	69
280594	AB	W,G,S^{200}_{204}	75-120	73
310594	AB	W,G,S_{208}	80-120	62
010694	AB	W,G	75-105	59
030694	AB	G	55	13
160994	BC	W,G,S^{208}_{225}	25-37	62
210994	BC	G,W	25-37	70
220994	BC	G,W	24-37	74
210695	A	W,G	180-200	51

2. Observations

The observations were taken with the VLA between 1993 February and 1995 June, in configurations ranging from A to CD (Table 1). The area of this northern part of the survey consisted of 13×81=1053 pointing centres. Due to system failures and compact antenna configurations in combination with radio–frequency interference (RFI), useful data were obtained for only 965 (Fig. 1).

The full width at half maximum (FWHM) of the primary beam (PB) of the VLA antennae at 1612.231 MHz is $27'$. The data were taken in circular RR polarization, using a total bandwidth of 3.3 MHz (614 $\mathrm{km\,s^{-1}}$) and 255 spectral channels (separation 2.27 $\mathrm{km\,s^{-1}}$). Doppler tracking was used during the observations, transforming the velocities to the frame of the local standard of rest (LSR), so the spectral band was centred at $0\,\mathrm{km\,s^{-1}}$ for each pointing.

We used mostly 0137+331, or if necessary 1331+305, as the primary calibrator and 1822−096, 1911−201, 1751−253 and 1751+096 as secondary calibrators. On each field, an integration time of 10×30 sec was scheduled, with in general 300 baselines available for observing.

3. Data reduction

Data were reduced with the reduction package Miriad (Sault et al. 1995); five– and six–letter acronyms in capitals throughout this paper will indicate the Miriad programs we used. To make the data quality uniform across the whole survey area, only baselines with lengths between 5 kλ and 55 kλ were used (cf. Table 1). The primary and secondary calibrators were edited first with a custom–made RFI flagger WSRFI (see Sect. 3.1) and further by

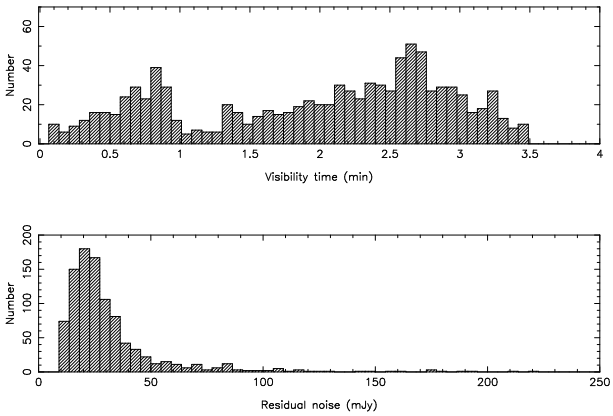

Fig. 3. a and b. These histograms display the net integration times and residual noises for all 965 fields used in the searching process (see Sect. 2). For each pointing 5 min integration time was scheduled.

hand. After calibration (MFCAL), the data from all pointings were edited only with WSRFI.

The searching was performed largely as described in Paper I, with MPFND, a custom–made derivative of INVERT, aimed at searching large amounts of modest–quality data for point sources. This routine Fourier–transforms spectral channels one by one, retaining only the position and flux density of the brightest pixel for each image. Subsequently, the peaks are correlated in the spectral direction, looking for statistically significant (OH/IR–type) spectral features. If one has been found, an appropriate point–source model is subtracted from the visibilities and the same routine is performed at a lower detection level. All details are given in appendix A of Paper I.

The image size was always 1665^2, with square cells of $1\farcs5$, searching all but 10 cells along each border. Four passes were performed, the last one well below $3\times$ the theoretical noise (as given by MPFND).

A few changes were made to accommodate specific properties of VLA data. To save time, with the VLA cubes three times larger than the ATCA cubes due to higher resolution, an extra first pass through the data was performed in the visibility domain. Spectral peaks were identified in the scalar–averaged spectra and then only the peak channel was Fourier transformed to find the source position.

With the modest spectral resolution of the VLA correlator, a large fraction of the sources induced spectral aliassing; the narrowest, mostly brightest, sources creating responses in all 255 channels. Obviously, these reponses may be negative. To account for this, we adapted the subroutine UVSUB to allow for negative point source models. Input models for the new UVSUB were "log" output files from UVSPEC, containing the *real* part of the visibilities, offset to the source position, for the whole spectral range (215 channels in calibrated data). Hence, in all passes, once a source position was established, either directly as a real source or after shifting to the real position in the case of detecting a sidelobe (see Paper I), a full spectral point–source model was subtracted from the visibility data. This clearly took out the random noise at the source positions as well, but the data on the whole were not significantly influenced.

The visibility–based point–source subtraction was not as effective for the VLA data as for the ATCA, due to the non–negligible third dimension in the antenna–position coordinates (u,v,w) for the VLA. Sources at higher offsets were occasionally redetected in later passes. This was corrected for in the post–searching cross–identification process.

3.1. Radio–frequency–interference excission

Three kinds of RFI corrupted the data during most of the observing dates. One was the usual broad–band Glonass RFI ('G' in Table 1), often accompanied by a single–channel spike ('S', sub–/superscripts indicating channel of spike). The third was interference from a nearby military base ('W'), depending in strength on u–v direction rather than baseline length, which saturated the correlator to give non–random noise characteristics (see Fig. 2).

The routine UVLIN, used for the ATCA data (Paper I,II), had no positive effect when applied to these data with the required high order of polynomial, probably again due to the non–negligible third dimension of the VLA array. However, with a custom–made visibility–flagging algorithm WSRFI, written for use within Miriad, we managed to excise the worst of all three types of RFI. In Fig. 2, we show the spectrum of one of the primary calibrators before and after running WSRFI on the data.

With the combined losses due to antenna downtime, data flagging to delete interference and retaining only baselines between 5 kλ and 55 kλ, the resulting net 'visibility time' (all visibilities used divided by the number of baselines used, times 30 sec) is of the order of 1–3 min (Fig. 3).

4. Results

The source tables and spectra (Table 2 and Fig. 10 can be downloaded from http://msowww.anu.edu.au∼msevenst/pubs.html

In Table 2 all narrow–line OH sources found are listed. In total there are 286 sources, 125 of which have been identified with known OH–1612–MHz masers. Ten sources have only one spectral peak. A reliable (see Sect. 5.5 for definition) IRAS identification is found for 207 sources. The median 'residual' rms–noise level is 25 mJy (Fig. 3, Sect. 5.1.1).

For each source the table gives an entry number (column 1), the OH$\ell - b$ name (column 2), observing date (column 3, see Table 1), position in J2000 coordinates (columns 4,5), the formal positional error (column 6) – much smaller than the actual error (Sect. 5.2) –, the dis-

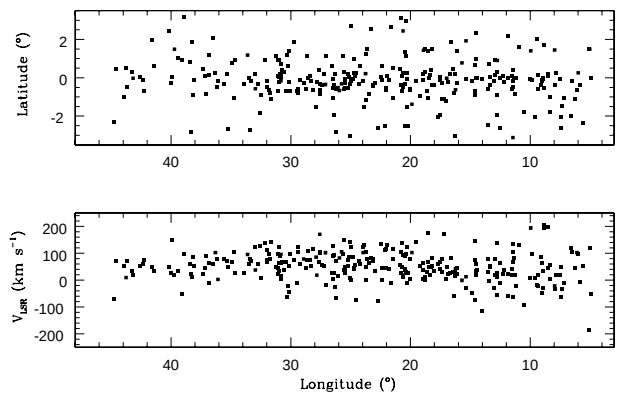

Fig. 4. a and b. The longitude–latitude diagram and longitude–velocity diagram for the 286 sources of Table 2. The central velocities (column 10) are plotted.

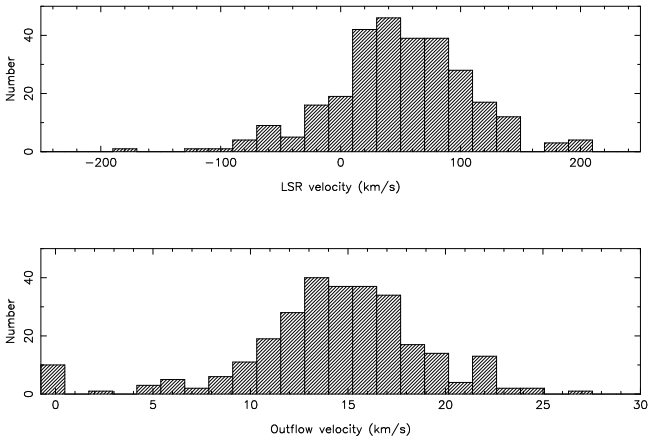

Fig. 5. a and b. The histograms of the central velocities and outflow velocities for the 286 sources of Table 2.

tance from the source to the pointing centre (column 7), the peak, stellar and outflow velocities (columns 8 to 11), the peak fluxes (column 12,13), calibration flag (see Sect. 5.3) and error in the peak flux density (column 14; see Sect. 5.3), the empirical residual noise in the field where the source was detected (column 15), presence of previous OH detection and the name of the nearest IRAS point source (column 16) and the distance to this nearest IRAS point source expressed as a fraction of the corresponding IRAS error ellipse (column 17).

The spectra for all sources are shown in Fig. 10. They are displayed with 50 $\mathrm{km\,s^{-1}}$ on either side of the velocity range of each object. The spectra were extracted from cleaned (128^2 $1''$ pixels around the source position) and restored cubes, summing over 3×3 pixels around the peak pixel. Only spectra #237 and #280 were extracted from raw cubes, as cleaning was impossible due to the awkward beam shape. No 'continuum fitting' other than the described RFI excision (Sect. 3.1) was applied (cf. spectra #097,104,253,275,280).

Dots over peaks in the spectra give an indication of the velocity range of the detections; note eg. the sidelobe from spectrum #223 in spectrum #219. Sidelobes are still present in the spectra, as most confusing sources would be outside the cleaned area. Negative sidelobes are obvious in eg. spectra #127 (from #132), #150 (from #149) and in an unfortunate way in #222 (from #223). Note the extreme velocity coincidence of #159 and #172, as well as #242 and #244.

In Fig. 4 the longitude–latitude diagram and longitude–velocity diagram are shown and in Fig. 5 the histograms of central– and outflow velocity.

5. Data analysis

In this section we analyse the global completeness of the survey and discuss the statistical accuracy of the quantities given in Table 2. The discussion and figures follow closely that of the corresponding section in Paper I, but is adapted to treat some VLA–specific details. We will assume errors are normally distributed, unless stated otherwise.

5.1. Survey completeness

5.1.1. Noise levels

The empirical noise levels (defined as the rms in the of 215×1645×1645 cubes after the last pass of source subtraction) for all 965 fields are shown in Fig. 3. The median noise is 25 mJy (mean 32 mJy: the same as the ATCA Bulge region); 90% of the fields have noise levels below 50 mJy.

5.1.2. Detection levels

In this section we treat the global completeness of the sample. There was no absolute lower detection limit set in the searching routines (opposed to the strategy for the ATCA survey). The half–power beam width (HPBW) of the VLA antennae at 1612 MHz is $13\farcm5$. Approximately 55% of the total area of the VLA survey would be covered within the HPBW (this includes the fact that 8% of pointings are missing). For fields that are not on the boundary of the surveyed region, the largest possible offset from the nearest pointing for any source is $21\farcm2$, which corresponds to a primary–beam response (PBR) of 0.16 (Fig. 7a). In Fig. 6 we see that this typically guarantees that the main lobe of a detected source is measured to be stronger than any of its sidelobes, even in other fields, provided we cover the entire survey region with our image sizes (square in α, δ), which is the case where there are no gaps (Fig. 1). Note that the field separation is the absolute maximum, given the primary–beam response, to still guarantee proper identification of the main lobes of all sources. In fields at the perimeter of the survey region

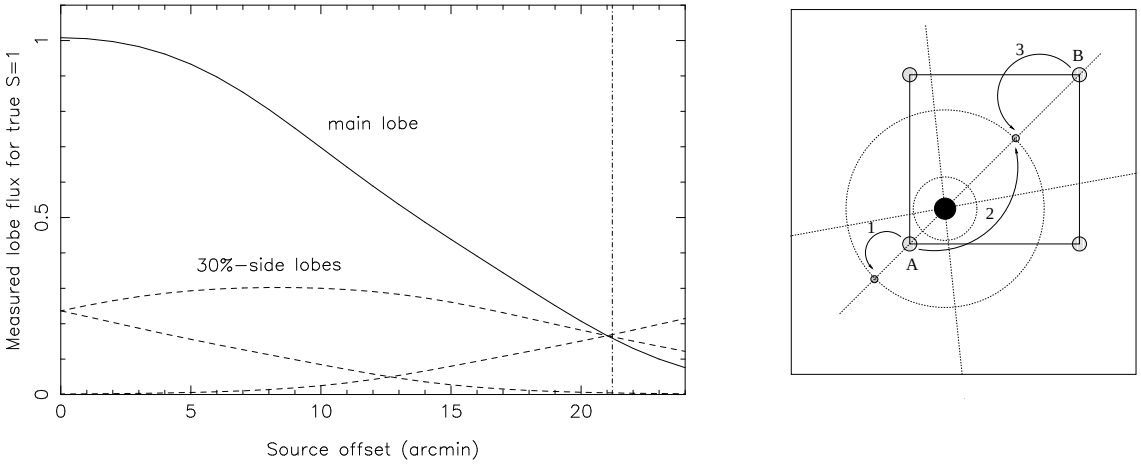

Fig. 6. A source (solid black circle in right panel) in the field of pointing centre A will create sidelobes in that field, as well as that of B ($42'$ away from A). The furthest strong (30%) sidelobe of a typical synthesized beam in the VLA survey is at $\sim 500''$ (small hatched circles). In the left panel, the response to a unity–flux–density source is given in the main lobe (solid curve) and in this furthest sidelobe, which we take to be on a spoke of the beam that runs through A and B, to calculate the extreme case. The dashed curves, from top to bottom at offset $< 12'$) give the response in the lobe offset towards A (1), away from A (2) and the latter seen from B (3), all using the known VLA primary–beam attenuation. The vertical line indicates the largest possible offset of sources detected in fields that are not on the boundary of the survey region. Only for sources on the very edge of a field, the main lobe of the synthesized beam is no longer observed to be brightest point.

(cf. Fig. 1), sources could be found in principle at offsets up to $29'$. In practice, the largest offset was $21\farcm3$ (Table 2); only four sources were found more than $20'$ away from the nearest pointing centre.

In Fig. 7b we plot the PBR of each source against its peak flux density. The solid line connects stars with the lowest detected OH flux densities, determined in bins of PBR. The dashed curve indicates the expected relation between PBR and flux–density cut–off for an absolute detection limit of 120 mJy (cf. 160 mJy, 140 mJy for the ATCA survey regions). Note that the empirical detection level is clearly not as constant across the VLA region as across the ATCA regions. The global limit is closer to 150 mJy, but there are a few detections that clearly are outliers (limit 90 mJy). This is due to the gaps in the coverage, that increase the area covered by large offsets from what it would normally be, combined with a larger spread in the noise levels (see above; Fig. 3).

In Fig. 7c we plot the cumulative flux–density distributions for all detected sources with PBR > 0.8 (solid) and, for comparison, with PBR < 0.6 (dashed). We postulate that the survey is essentially complete for PBR > 0.8, for flux densities above the sensitivity limit, and take the solid curve in Fig. 7c as the intrinsic cumulative flux–density distribution for the present sample. We use this distribution to determine the fraction of the 'flux–density function' seen at a given offset (Fig. 7d), with the absolute limit of 120 mJy to determine the cut–off in flux density at the offset. In short, the curve in Fig. 7d shows what fraction of the flux–density distribution we see if we select sources with a certain offset from Table 2.[2]

The solid curve in Fig. 7e shows what fraction of the searched area we cover if we select all sources with a certain flux density from Table 2. The dashed curve in Fig. 7e shows the same distribution, but this time properly corrected for the gaps in the coverage and the corresponding redistribution of area from small offsets to large offsets. The dashed curve reaches 99% completeness for 2 Jy, the solid curve for 0.5 Jy. The latter is virtually the same as the 99% completeness of the ATCA surveys. The survey is 80% complete for sources of 320 mJy or 285 mJy, respectively, again similar to the ATCA surveys. This should be interpreted as follows. If we select all sources brighter than 2 Jy (after correction for PBR), the distribution on the sky will be entirely uninfluenced by our observations and only reflect the real surface–density distribution. If we select all sources brighter than 0.5 Jy, the distribution will show holes at the missing pointings, but will not be influenced by the variable sensitivity within fields. If one selects even fainter sources, the distribution will be a complicated function of both intrinsic surface density and survey sensitivity.

Finally, in Fig. 7f, we plot the signal–to–noise ratio for all detected sources against offset. The limiting signal–to–

[2] Note that the text of Paper I describes this plot incorrectly; the area covered by points of that given offset is *not* taken into account. The actual plots in Paper I,II are the same as in the present paper.

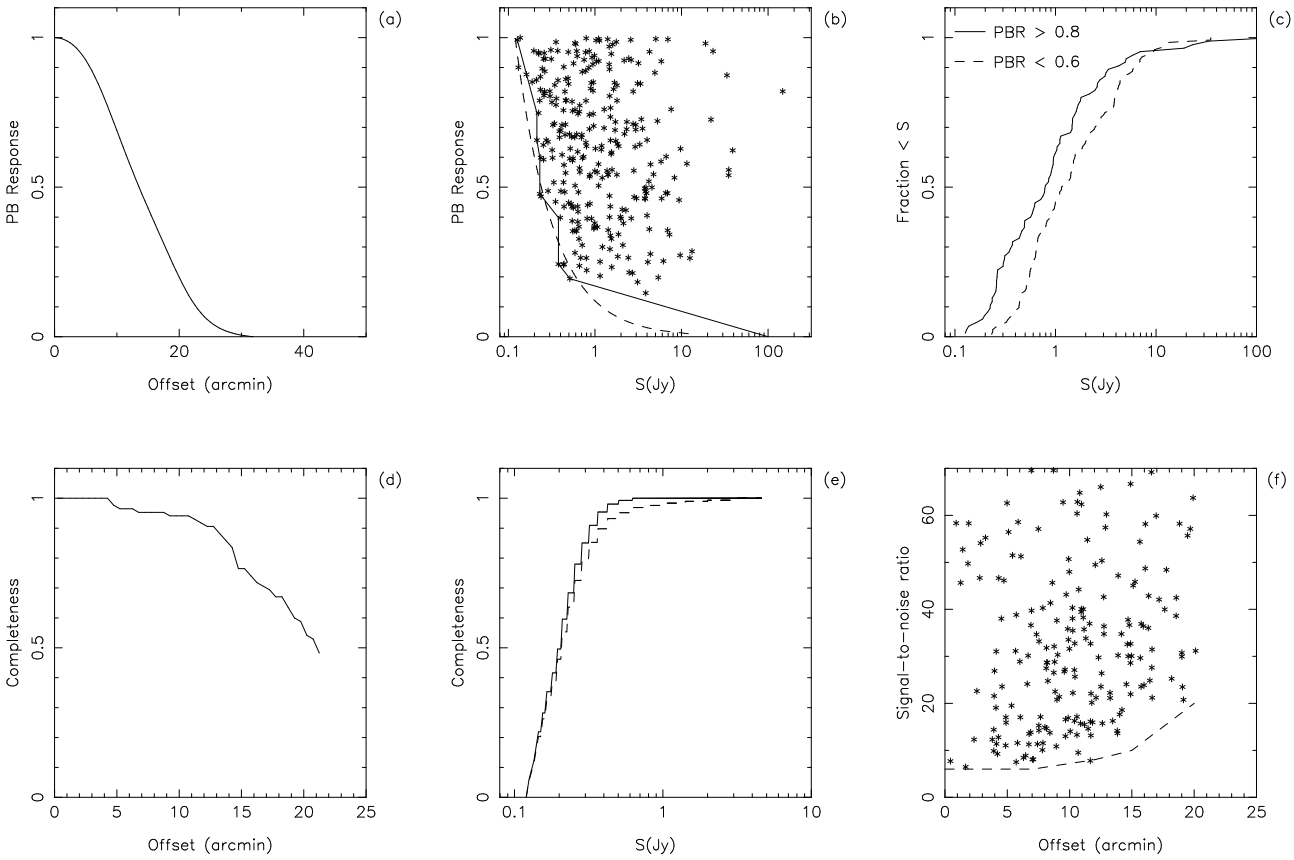

Fig. 7. a–f. Representation of the completeness of the data (Sect. 5.1.2). **a** The primary beam response (PBR) of the VLA antennae at 18 cm, as a function of radial offset from the pointing centre, taken from Napier & Rots (1982). **b** The PBR calculated for the detected sources plotted against the highest peak–OH flux densities, corrected for primary beam attenuation. The solid line indicates the lowest flux densities detected in PBR bins. The dashed line indicates the expected inner boundary calculated from the PBR curve in (a) for a limiting flux density of 120 mJy (chosen to fit observed extremes). **c** The cumulative flux density distribution for stars with PBR values > 0.8 (solid line) and < 0.6 (dashed line). The solid line is taken to be the intrinsic OH flux density distribution for the sources in the survey. **d** The completeness, relative to the pointing centres, of the survey as a function of position offsets from the field centres. **e** The completeness of the sample as a function of flux density. The offset out to which a source with certain flux density can be observed is determined from the dashed line in (b). Then we determine the area covered inside that offset, as a fraction of the total area of the survey. The solid curve gives this for the ideal case of no missing pointings, the dashed curve takes the gaps (Fig. 1) into account. **f** The signal–to–noise ratio for all sources, plotted against their radial offset from the pointing centre. The dashed line shows the (observed) lower limit at a certain offset.

noise ratio is 7 (the corresponding ratios for the ATCA surveys are 4 and 6, respectively) at low offsets.

Summarizing, the lower sensitivity limit is 120 mJy ± 30 mJy, with the most sensitive detections made at 7σ. The survey is 99% complete for flux densities higher than 0.5 Jy (or 2 Jy, when taking into account holes in the survey area) and 90% complete in flux density for offsets lower than $13\farcm2$.

5.2. Positions

The positions given in Table 2 (columns 4,5) are determined by fitting a parabola over 3×3 $1''$ cells around the peak pixel in the cleaned and restored map of the peak channel (MAXFIT), made around the position of the object found by the searching routine. This ensures that the inaccurate handling by Miriad of the third coordinate of the visibility domain does not influence our final positions. The errors in Table 2 (column 6) are the formal errors determined by fitting a point–source object (IMFIT) to the centre of the above–mentioned map. They are typically negligible with respect to the errors introduced by the low resolution of some of the observations.

Firstly, the positional accuracy varies dramatically from source to source, as the maximum baseline length varies from 7 kλ (see Table 1) to 55 kλ , corresponding to a resolution of $29''$ and $4''$, respectively. With $1''$ cells for the imaging of all fields, the positional errors for sources

observed with the lowest resolution would go to infinity (see Fig. 5 in Paper I). As an example, for a maximum baseline length of 25kλ the half width of the synthesized beam at half maximum would be $\sim 8''$, or 5.5 cells, giving an error of <2 cells or $2''$, following Fig. 5 in Paper I.

Secondly, since we discard baselines below 5 kλ (Sect. 3), for observations with compact array configurations (Aug,Sep 1993) the synthesized–beam shape was severely compromised, given the minimal hour–angle coverage (cf. #237,280 with infinite beam size). However, our position for #280 differs only $11''$ of that given in the literature (Braz & Epchtein 1983), which is entirely within their errors.

In short, the typical error in the positions is of the order of $2''$, in agreement with our findings in Sect. 5.7.

5.3. Flux densities

The flux densities in Table 2 (columns 12,13) were determined from the same cubes as described in Sect. 5.2 . The data were summed over 3×3 $1''$ cells around the maximum cell and divided by the corresponding sum of the synthesized beam (IMSPEC). The formal errors (column 14) were determined by IMFIT, in the peak channel. Errors marked with $*$ (mostly 0.0 mJy) indicate that the absolute flux–density calibration was not carried out properly in the corresponding field. We applied a fudge factor of 16 to all flux densities measured in those fields, which introduces an error of 25% for those sources (in properly calibrated fields this factor ranges from 12 to 20). In all other fields, the error from the absolute calibration is of the order of 1% , except for those observed on 260594 where it is 20% . From the time–dependent calibration solutions, we expect errors of 10% – 20% in the flux densities.

An addional error is introduced by random noise and binning. In Fig. 8c we show that this amounts to 35% (binning) ± 5% (noise). The corresponding errors in the peak–flux–density ratio (Fig. 8d) is ∼20% (0.7/0.6 instead of 1/1, Fig. 8c).

Summarizing, the relevant errors are on average 15% (calibration) plus 5% (noise) plus for some sources 25% (fudging). Multiplying, we find a typical accuracy for the flux densities in Table 2 of 20% , which is in agreement our findings in Sect. 5.7 , or 40% for fudged sources.

5.4. Velocities

As the VLA has on–line Doppler tracking, the velocity band is always centered on 0 $\mathrm{km\,s^{-1}}$ (LSR), but the bandpass calibration, in frequency space, changes the velocity range slightly with position and date. However, all detections are within the range that was covered on all dates (-200 $\mathrm{km\,s^{-1}}$, $+210$ $\mathrm{km\,s^{-1}}$), so sensitivity and errors are independent of the value of the velocity.

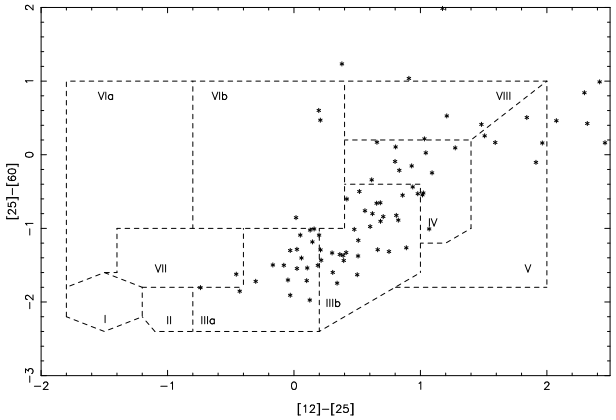

Fig. 9. The IRAS two–colour diagram for sources with an IRAS identification lying within the IRAS error ellipse (column 17, $N \leq 1$) with well–determined IRAS 12, 25 and 60 μm flux densities (i.e. no upper limits). The colours are defined as [12]-[25]≡2.5 $^{10}\log(S_{25}$ / $S_{12})$.

In Fig. 8a we show the difference between measured stellar velocity, combining the effects of binning, noise and aliassing, and the true stellar velocity of a perfect spectrum, as a function of true stellar velocity with respect to the centre of the channel of detection. The typical errors are less than 1 $\mathrm{km\,s^{-1}}$, in agreement with our finding in Sect. 5.7 .

The same arguments as given in Paper I apply, that for double–peaked sources the outflow velocity will be systematically slightly underestimated (see also Fig. 8b) due to undersampling of the spectra. For single–peaked sources there is an uncertainty in the *stellar* velocity of typically 14 $\mathrm{km\,s^{-1}}$. The fraction of such single–peak sources in this VLA set is low (3%) compared to the ATCA sets in Paper I,II (9%,18%). Due to the variable data quality and remnant RFI, fewer single–peaked detections were significant according to our criteria. For instance, a detection in three separate channels at the same spatial position was more readily accepted if it was in two neighbouring channels plus one at a certain velocity interval than if it was in three neighbouring channels, even if statistically those two scenarios may have the same probability. Empirically, the single–peaked configuration is more likely to turn out not to be a source, but remnant RFI.

5.5. IRAS identifications

In column 17, the distance from the OH source to the position of the IRAS point source (column 16) is given in fractional radii of the IRAS error ellipse in the direction of the OH position (see Paper I). $N = 1$ means the position of the OH source can be identified with the position of the IRAS source with 95% confidence. The IRAS PS in column 16 is in fact the one that is most likely to be connected to the OH source, ie. with the smallest value of N .

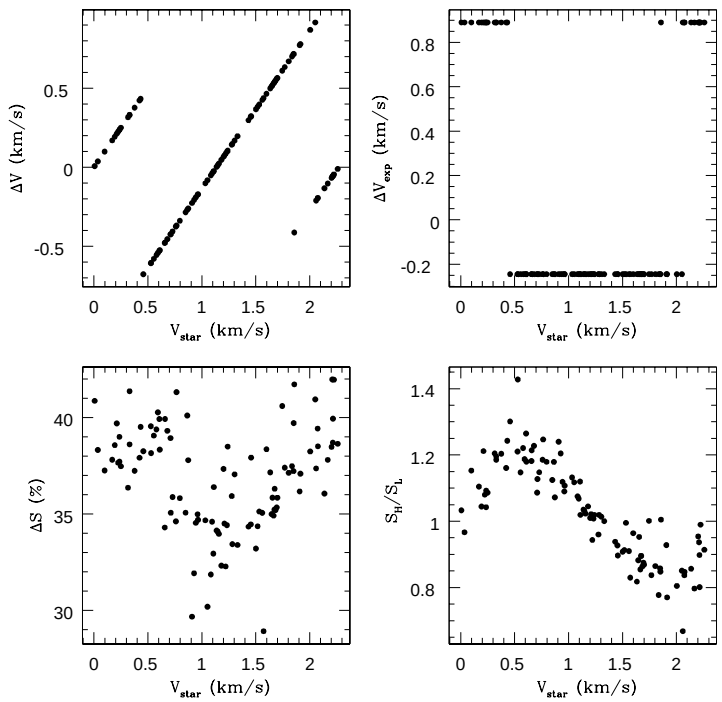

Fig. 8. a–d. With the channel width of $2.27\,\mathrm{km\,s^{-1}}$, the intrinsic velocity structure of the maser features, of order 0.2 $\mathrm{km\,s^{-1}}$ wide, is undersampled. Hence, aliassing and measurement errors are introduced, that depend on the offset of the true spectral peak from the centre of the channel it is detected in. This figure gives the difference between 'measured' and 'perfect' OH/IR–type spectrum in stellar velocity (**a**), outflow velocity (**b**), flux density (**c**) and peak–flux–density ratio (**d**). The 'perfect' spectrum has an outflow velocity 15 $\mathrm{km\,s^{-1}}$ and unit flux density for both peaks. We 'observed' it 100 times, adding random noise so that the resulting signal–to–noise ratio was between 0.0 and 0.3, shifting the stellar velocity (abscissae) by random amounts within one channel width, convolving with the spectral–response sinc function and binning to the resolution of the observations. The combined errors are ± 0.8 $\mathrm{km\,s^{-1}}$ in velocity, mostly -0.24 $\mathrm{km\,s^{-1}}$ in outflow velocity (independent of the value of the outflow velocity) and of the order of +35% in flux density (the measured value is lower than the true one, mostly due to the wide bins) with ±5% due to noise and aliassing. In the fourth plot we see that the intrinsically symmetric spectrum may be distorted by $> 20\%$. None of these quantities show any trend with signal–to–noise ratio.

Of the 286 sources, 207 (72%) have an IRAS PS counterpart within the IRAS error ellipse ($N < 1$). This fraction is comparable to those found in Paper I,II (65%,75%), as well as to the 68% found by Blommaert et al. (1994). In Fig. 9 we show the IRAS two–colour diagram (van der Veen & Habing 1988) for sources with an IRAS identification with $N < 1$ and reliable IRAS colours.

Note that this two–colour diagram is very similar to that of the ATCA Bulge OH/IR stars (Paper I), rather than of the ATCA Disk stars, in terms of the population of region V and the scatter on the evolutionary track (regions III). This similarity remains the same when leaving out the source with longitude below 10°. It could be due to the orientation of the Bar, that causes it to extend to higher longitudes in the northern galactic plane. However, it should be realized that by plotting only those sources that have well–determined IRAS flux densities in three bands, a selection effect is introduced. The distribution is influenced by the levels of background confusion.

5.6. OH identifications

We searched the SIMBAD data base for previous OH detections within $1'$ from each position in Table 2. In column 16, as well as in Fig. 10, an '$*$' indicates a reference to Paper I; if not in that catalogue, an 'x' indicates a reference to te Lintel et al. (1989); if not in that catalogue, a '+' indicates another OH reference and a '−' no OH reference at all. In total, there are 26 '$*$' references, which is one less than determined from the actual Paper I source list (see next section) since entries in SIMBAD are not always entirely correct. Note that we did not check for coincidence in velocity. By this definition, 161 sources in Table 2, or 56% (cf. 47,55% for the ATCA survey regions), are new detections; see Paper I for a more elaborate discussion.

5.7. Overlap with the ATCA survey

The strip of $4°.8 < \ell < 10°.2$ was observed in both the VLA– and the ATCA parts of the survey, to allow direct comparison between the two resulting data sets. In that region, there are 47 stars detected in the ATCA survey and 36 in the VLA survey, of which 27 stars are actually in common. With another two sources in common between the two parts of the ATCA survey (Paper I,II), the total number of sources in the combined survey is 766.

Taking into account the intrinsic variability of the sources and the varying primary–beam responses in systematic observations, even two surveys with exactly the same flux–density limits would not yield the same detections unless they were carried out simultaneously and with the same pointing pattern. The redetection rate of the VLA is 27/47=57% and of the ATCA 27/36=75% . The difference between those numbers is a direct mea-

sure of the relative "efficiency" ((number of detected sources)/(number of detectable sources within limits)) of the two surveys, provided the overlap region is representative of the whole area. The ATCA survey is 30% more "efficient" than the VLA survey. This is entirely in agreement with the ratio of FWHM coverages : the ATCA Bulge survey covers 73% of the survey area within a PBR of 0.5, the VLA 55% , including the missing pointings.

If we compare this VLA data set to the ATCA Disk data set, there are 250 and 202 stars, respectively, in the strips from $\pm$ 10° to $\pm$45° in longitude, even though VLA survey is less efficient. This could again be interpreted as a sign of the Bar extending to much higher longitudes on the northern side of the galactic Centre (see Sect. 5.5).

For the 27 sources in common, the average difference in position is $1\farcs66$ ($0\farcs04$ – $2\farcs91$) and in velocity $0.68\,\mathrm{km\,s^{-1}}$. The latter value excludes two sources (#010=SCHB268, #021=SCHB286) for which one of the two peaks was not detected in the ATCA survey and source #020 (SCHB285) which is known to have a very variable velocity profile (Sevenster & Chapman in preparation).

For 8 sources, the observing date (200293) was relatively close to that of the ATCA, so that a flux–density comparison could be made. Taking into account the differences in velocity resolution and the typical variability of sources, the flux densities are the same to about 20% (cf. Sect. 5.3).

6. Summary

We have given the results of a survey of the region $5° \leq \ell \leq 45°$ and $|b| \leq 3°$ in the OH 1612.231 MHz maser line. The survey is 99% complete for sources brighter than 500 mJy and 90% complete for positional offsets from the pointing centres smaller than $13'$. The absolute flux density limit is ∼120 mJy. We have found 286 compact OH–maser sources, 161 of which are new detections. The sources are mainly OH/IR stars, with a few related sources, like planetary nebulae. The positions are accurate to $2''$, the velocities to 1 $\mathrm{km\,s^{-1}}$ and the flux densities to 20% . For 207 sources, an associated IRAS point source is found. The total number of sources in the combined ATCA/VLA survey is 766.

The VLA survey is similar to the ATCA surveys in terms of global completeness statistics, but considerably less homogeneous in quality. The efficiency is approximately 75% that of the ATCA Bulge survey. The biggest differences are the considerably worse accuracy in the flux densities and the very low fraction of single–peaked sources. Signatures of a higher fraction of bar–like stars in this part of the survey than in the ATCA Disk survey are found in the surface number density of detected sources and arguably in the IRAS two–colour diagram.

Acknowledgements. This research has made use of the Simbad database, operated at CDS, Strasbourg, France.

References

Blommaert J., van Langevelde H., Michiels W., 1994, A&A, 287, 479

Braz A., Epchtein N. 1983 , A&AS, 54, 167

Habing H.J., 1996, ARA&A, 7, 97

Napier P., Rots A., 1982, VLA Test memorandum no.134

Sault R.J., Teuben P.J., Wright M.C.H., 1995, In: Shaw R., Payne H., Hayes J. (eds.) PASPC 77, Astronomical Data Analysis Software and Systems IV, p. 433

Sevenster M.N., Chapman J.M., Habing H.J., Killeen N.E.B., Lindqvist M., 1997a, A&AS, 122, 79 (Paper I)

Sevenster M.N., Chapman J.M., Habing H.J., Killeen N.E.B., Lindqvist M., 1997b, A&AS, 124, 509 (Paper II)

te Lintel Hekkert P., Versteege-Hansel H.A., Habing H.J., Wiertz M., 1989, A&AS, 78, 399

Van der Veen W.E.C.J., Habing H.J., 1988, A&A, 194, 125

Table 2 Compact OH–maser sources in the northern galactic Disk region (obtain from http://msowww.anu.edu.au∼msevenst/pubs.html)

The columns of Table 2 contain the following information :

1 Sequence number (coincident with spectra in Fig. 10)
2 Name in the OH$\ell - b$ convention
3 Date of observation. Date '000000' means data were taken during more than one observing run (see Table 1 for parameters)
4 Right ascension of the brightest peak for epoch J2000 (typical error $2''$, Sect. 5.2)
5 Declination of the brightest peak for epoch J2000 (typical error $2''$, Sect. 5.2)
6 Formal measurement error in position from IMFIT (determined in the channel of the brightest peak) in arcsec (Sect. 5.2)
7 Radial offset of the source from pointing centre in arcmin
8 Line–of–sight velocity with respect to the LSR of the blue–shifted (L) peak. For single–peaked spectra the velocity of the peak is always given as blue–shifted for reasons of tabulation (typical error 1 $\mathrm{km\,s^{-1}}$, Sect. 5.4).
9 Same for the red–shifted (H) peak (typical error 1 $\mathrm{km\,s^{-1}}$, Sect. 5.4).
10 Stellar velocity (typical error 1 $\mathrm{km\,s^{-1}}$ / 14 $\mathrm{km\,s^{-1}}$, Sect. 5.4).

$$v_\mathrm{c} = 0.5 \cdot (v_\mathrm{H} + v_\mathrm{L})$$

11 Outflow velocity; zero for single–peaked sources (typical error 1 $\mathrm{km\,s^{-1}}$, Sect. 5.4).

$$V_\mathrm{exp} = 0.5 \cdot (v_\mathrm{H} - v_\mathrm{L})$$

12 Flux density in image domain at peak pixel of cleaned, restored image (IMSPEC), corrected for primary–beam attenuation, but not for any 'continuum' of the blue–shifted (L) peak (typical error 20% , Sect. 5.3).
13 Same for the red–shifted (H) peak (typical error 20% , Sect. 5.3).
14 Formal measurement error in flux density, determined in the channel of the brightest peak (IMFIT). An asterisk indicates that the corresponding field was not calibrated properly (Sect. 5.3)
15 Empirical noise in 'empty' cube for the present field (Sect. 5.1.1, channel width 2.27 km/s)
16 A '+','∗' or 'x' for a, or '−' for no, OH identification within $1'$ in the Simbad database (Sect. 5.6), and the IRAS PSC position with highest identification probability (ie. smallest N, see column 17, Sect. 5.5)
17 Ratio between the size of the error ellipse of, and and the distance to, the IRAS PS of column 16, in the direction of the OH position (Sect. 5.5)